Parametric aqueous electrodeposition study and characterization of Fe–Cu films

Evangelia Dislaki[a], Jordi Sort[a,b,*], Eva Pellicer[a, §]

[a] Departament de Física, Universitat Autònoma de Barcelona, E08193 Bellaterra, Spain.

[b] Institució Catalana de Recerca i Estudis Avançats (ICREA), Pg. Lluís Companys 23, E08010 Barcelona, Spain.

To whom correspondence should be addressed: *jordi.sort@uab.cat; §eva.pellicer@uab.cat

Keywords: Fe-based alloy, Cu-based alloy, co-deposition, electroplating, magnetic properties

Abstract

In this study, Fe_xCu_{1-x} films over a wide composition range ($0 \leq x \leq 86$) were prepared from an aqueous sulfate electrolytic solution using three different complexing agents and variable plating conditions. The effect of parameters such as bath composition, current density and temperature on the elemental composition, morphology, structure and magnetic properties of the deposits was investigated. The electrochemical behavior was studied using cyclic voltammetry. High quality, smooth deposits with good substrate adhesion and minimized oxygen content were achieved. X-ray patterns indicate phase separation, though results from Rietveld analysis strongly suggest partial alloying. Magnetization dependence on Fe content is clearly demonstrated.

1. Introduction

The Fe_xCu_{1-x} alloy has attracted tremendous interest with respect to the magnetism of the face-centered cubic (fcc) phase of Fe (austenite), which can be obtained either via precipitation in a

Cu matrix [1-3] or can be epitaxially grown on a Cu substrate [4-5]. However, the mutual solubility of Fe and Cu is quite low due to their positive enthalpy of mixing which has a theoretical value of 10.5 kJ mole^{-1} [6]. Only ≈4 at% Fe can be dissolved into the Cu matrix with fcc structure and, conversely, ≈10 at% Cu can dissolve into the Fe matrix with body-centered cubic (bcc) structure near their respective melting points [7]. Metastable solid solutions have been prepared by different approaches, such as mechanical alloying [8-14] and physical vapor deposition techniques [15-17]. Single crystalline Fe_xCu_{1-x} alloys over the entire composition range have been prepared successfully on a GaAs (001) substrate via molecular beam epitaxy for film thicknesses up to 8 nm [18]. Studies on the magnetic coupling and alloying interface effect of Fe–Cu multilayers [19-21] and superlattices [16] and [22] have also been carried out with potential applications in giant magnetoresistive (GMR) devices.

Electrodeposition offers an attractive alternative due to its simple, cost-effective and easy to operate set-up. Moreover, it works at ambient pressure and enables the growth of relatively thick homogeneous coatings at fast deposition rates. The properties of deposits can be fine-tuned by modulating factors such as the composition, temperature and pH of the electrolytic bath and electroplating parameters such as agitation and deposition mode. However, due to the immiscibility of the system and the tendency of Fe to form oxides/hydroxides, existing literature related to Fe–Cu films prepared via electrodeposition is somewhat limited in scope. In few works, a relatively wide composition range of partially alloyed deposits of nanometer-thickness has been obtained by varying either the Cu or Fe salt concentrations [23-24]. This method was also used in one study focused on achieving high physical properties and enhanced corrosion resistance of thick coatings [25]. In another case, Mössbauer studies of metastable FeCu alloys in powder form targeted four different compositions attained by altering the Fe salt concentration

[26]. Alternatively, the applied potential during pulsed electrodeposition mode was tuned in one study to produce the desired thin film composition and the magnetic behavior was investigated in relation to Fe content and temperature [27]. In another paper, Mössbauer studies were performed specifically on the CuFe alloy in powder form with a 72 at% Fe [28]. A paper on the electrodeposition of Cu-rich CuFe thin foams for supercapacitor electrodes was concentrated on the specific capacitance, the electrochemical response and the effect of thermal conditioning [29]. Finally, the effect of magnetic fields parallel to the electrode surface during deposition on the morphology and composition of the thin films has been reported [30].

Additionally, the results of studies on the structural and magnetic properties vary significantly since these are dependent on the fabrication method and the experimental conditions. Importantly, the Fe concentration below which a single fcc structure is obtained, the concentration range of mixed bcc and fcc phase and the Fe concentration above which a single bcc phase is observed, differs for each fabrication method.

In this work, we have prepared micrometer-thick Fe_xCu_{1-x} films over a wide composition range ($0 \leq x \leq 86$) from three electrolytic solutions where a different complexing agent was used. Subsequently, extensive characterization of the composition, morphology, structure and magnetic properties of the deposits obtained was carried out. Optimized synthetic conditions leading to Fe-rich films with minimized oxygen content are highlighted.

2. Experimental

2.1 Instrumentation

Electrodeposition was performed in a three-electrode cell connected to a PGSTAT302N Autolab potentiostat / galvanostat (Ecochemie). A double junction Ag|AgCl (E = +0.210V/SHE) acted as reference electrode (RE) (Metrohm AG) with a 3M KCl inner solution and a 1M Na_2SO_4 outer solution. A Pt wire was used as a counter electrode (CE). Silicon/silicon dioxide (SiO_2) substrates with a 10 nm Ti adhesion layer and a 90 nm Au seed layer served as the working electrode (WE) for deposit growth and for cyclic voltammetry (CV) studies. The working area was measured to be 0.25 ± 0.01 cm^2.

2.2 Chemicals and electrolytic solutions

The electrolytes (100 mL) were prepared with Millipore Milli-Q water and ACS Reagent grade chemicals purchased from Sigma-Aldrich. The first solution contained 58.8 g/L $(NH_4)_2Fe(SO_4)_2{\cdot}6H_2O$, 1.25 g/L $CuSO_4{\cdot}5H_2O$ (i.e., a [Fe(II)]/[Cu(II)] molar ratio of approximately 30), 20.2 g/L citric acid as a complexing agent, 0.2 g/L sodium dodecyl sulfate as a wetting agent and 0.46 g/L saccharine as a grain refining agent (bath A). The as prepared pH was 2.2 and samples were deposited at discrete working temperatures of 25 °C, 35 °C and 45 °C. For the second solution 7.9 g/L glycine was used instead as a complexing agent (keeping the concentration of complexing agent at 0.1M) and the pH was adjusted from 3.7 to 2.2 with addition of H_2SO_4 (bath B). Finally, for the third solution, 22.9 g/L sodium gluconate was the complexing agent and samples were deposited both from the as prepared solution with a pH of 4.1 (bath D) and after the adjustment of the pH to 2.2 with the addition of sulfuric acid (bath C). The stability of the solutions has been confirmed over the course of at least a few months.

2.3 Electrode preparation and procedure

Before electrodeposition, substrates were cleaned with acetone, followed by isopropanol and, finally, rinsed with Milli-Q water to remove any debris and residues. The electrolyte was deaerated with argon gas before each deposition and mild stirring was applied by means of a magnetic stirring bar (ω = 200 rpm). The galvanostatic mode was chosen for deposition with applied current densities in the range of -25 mA cm^{-2} to -100 mA cm^{-2}.

2.4 Characterization

Sample morphology and roughness were observed via Scanning Electron Microscopy using a Zeiss MERLIN field emission scanning electron microscope (FE-SEM) and Confocal Laser Scanning Microscopy (CLSM) with the confocal 3D optical surface metrology system LEICA DCM3D, respectively. The elemental composition was determined by Energy Dispersive X-ray Spectroscopy (EDXS) at an acceleration voltage of 15 kV. The mass of the deposited material (Fe and Cu amounts) was determined using a Perkin Elmer Optima 4300DV Inductively Coupled Plasma Optical Emission Spectrometer (ICP-OES). In preparation, the deposits were dissolved in test tubes containing 2 ml of nitric acid solution and one tube was filled solely with the solution to be used as a reference. The crystallographic structure of the deposits was studied by X-ray Diffraction (XRD). The XRD patterns were recorded on a Philips X'Pert diffractometer using CuK_{α} radiation and a Bragg-Brentano θ-2θ configuration. Cell parameters, crystallite sizes and microstrains were evaluated by Rietveld refinement using the Materials Analysis Using Diffraction (MAUD) software [31]. In order to determine elemental oxidation states, X-ray Photoelectron Spectroscopy (XPS) analysis of several samples was carried out on a PHI 5500 Multitechnique System spectrometer from Physical Electronics, equipped with a monochromatic X-ray source placed perpendicular to the analyzer axis and calibrated using the $3d^{5/2}$ line of Ag. The adventitious C1s line at 284.5 eV was used as a charge reference to calibrate the XPS spectra. Measurements for the composition depth profiles of six selected samples were obtained by sputtering the surface with an Ar^+ ion source for 2 minutes (~10-15 nm below the surface). The energy of the deconvoluted peaks was compared with the NIST XPS database. A linear background removal method was employed [32]. For the magnetic characterization samples were placed in a Vibrating Sample Magnetometer (VSM) from LOT-Quantum Design and hysteresis loops were recorded at room temperature, along the in-plane direction of the films, over an applied field range of -20 kOe to 20 kOe.

3. Results and discussion

3.1 Cyclic voltammetry studies

CV curves were recorded from all electrolytic solutions at different temperatures in order to determine the current density range suitable for deposition. A single cycle was run for each case with a scan rate of 0.05 V s^{-1} and the potential sweep was initiated at -0.2 V. Initially, the cathodic limit for bath A was varied between -0.8 and -1.3V to identify where the reduction and oxidation of different species occurs. Moreover, an additional scan was performed with the exclusion of the Cu salt while preserving a constant concentration of the metal cations in the solution, thus facilitating the interpretation of the anodic peaks (Fig. 1a). As is evident in Fig. 1b, the onset of deposition occurs at approximately -0.7 V. At higher cathodic limits, as the potential moves to more negative values, a steep increase in the absolute value of the current density is observed. A noisy signal indicates increased hydrogen co-evolution. After reversal of the scan direction, a single oxidation peak appears at cathodic limits lower than -1.1 V, attributed to Cu species (peak P1). This can be verified by comparing with Fig. 1a where there is only Fe present in the solution and, consequently, there are no observable peaks at the -0.8 V and -0.9 V limits. The onset of deposition for Fe takes place around -1 V and it can be seen that the Fe oxidation peak (peak P5) increases in intensity and shifts to the right for higher cathodic limits. Notably, as can be discerned from Fig. 1b, at the -1.1 V limit a broadened oxidation peak appears (peak P2), shifted to the left relative to peak P1, which signifies the existence of a mixed phase. At the -1.2 V limit, an increase in hydrogen co-evolution is remarked, accompanied by a shift of the oxidation peak P2 to the left and the appearance of a shoulder peak in the anodic scan (peak P3). Furthermore, a weak second oxidation peak appears (peak P4). When compared to the Fe oxidation peak 5 in Fig. 1a, peak 4 corresponds in position but is substantially broadened indicating once again the presence of a mixed phase. At the highest cathodic limit of -1.3 V, there is intense hydrogen co-evolution leading to introduction of significant amounts of oxides and hydroxides in the deposits. As result, a clear double-peak split (peaks P2 and P3) and a marked augmentation of peak P4 is seen in the anodic scan. These interpretations were in agreement with EDX elemental analysis.

After these preliminary tests, the cathodic limit was set to -1.5 V for all experiments. As seen in Fig. 1c, the onset of deposition at room temperature is similar for electrolytes A, B and C at about -0.7 V. As expected, in the anodic scan, a complex oxidation process takes place with multiple peaks denoting the formation of non-single phase deposits with variable chemical composition. According to the insights provided by this study an appropriate range of current densities was chosen for sample preparation.

With respect to the effect of temperature, similar trends where recorded for all electrolytes. As exemplified in Fig. 1d for the gluconate containing solution at pH=2.2 (bath C), the increase of temperature to 35°C and, subsequently, to 45°C leads to an earlier onset of deposition and faster deposition rates. This is seen by an increase in the absolute value of current density, which indicates rapid deposition of large amounts of material within a narrow potential range. Consequently, this is accompanied by an increase of the height of the oxidation peaks.

3.2 Effect of complexing agents, current density and temperature

The effect of current density on deposit composition for the different electrolytes at 25°C can be observed in Fig. 2. Error bars have been included, which represent the standard deviation for at least three replicas in each case. As expected, the increase of current density favors deposition of Fe, which is charge transfer controlled [33]. At large absolute values of current density, deposit composition becomes more difficult to control and oxygen incorporation increases in electrolytes A, B and C. This behavior suggests an increase in the local pH in the vicinity of the cathode, which, although mitigated by the inclusion of boric acid, results in hydrogen evolution reactions and possibly in the formation and precipitation of iron hydroxides on the cathode, which are incorporated in the deposit. When the value of current density exceeds -75 mA cm^{-2} for the citric acid (A) and glycine solution (B) and -100 mA cm^{-2} for the gluconate electrolyte (C and D) deposit quality rapidly declines and poor adhesion to the substrate occurs.

For the citric acid and glycine electrolytes (baths A and B), samples over a wide composition range are obtained, though glycine appears to favor deposition of deposits slightly richer in Cu (Fig. 2a and 2b). In the gluconate solution (baths C and D), the samples are mostly Fe-rich with more than 70 at% Fe. Copper-rich deposits are only obtained at current densities below -50 mA cm^{-2} as seen in Fig. 2c.

For comparison purposes, samples were also deposited with the as prepared pH for the glycine and gluconate electrolytes. In the case of glycine, at a pH value of 3.7, the deposit quality and substrate adhesion was extremely poor. For this reason, results from this bath were not considered. Contrarily, from the gluconate electrolyte fast deposition of high quality Fe-rich deposits was possible (bath D). Elemental composition was also easier to control at the 4.1 pH value across the entire range of applied current densities while oxygen incorporation was kept low. It is assumed that the gluconate ions in the solution act as an inhibitor to the deposition of Cu due to their complexion of Cu^{2+} via a ligand carboxyl group [34]. At lower pH the stability of the copper-gluconate complex is compromised, which increases the number of free Cu^{2+} ions and allows deposition of Cu-rich films at low current densities [34].

Next, the effect of temperature was studied by comparing the deposit composition at 25°C, 35°C and 45°C for the different electrolytes when plating at a current density of -50 mA cm^{-2}, as shown in Fig. 3. The increase of temperature improves mobility and, thus, favors the deposition of Cu, which is mass transfer controlled in the citric acid [35] and glycine solutions [36] (baths A and B). This is also accompanied by a decrease in the oxygen content, which is closely linked to the amount of Fe in the deposit (Fig. 3a and 3b). In the case of gluconate, the reverse trend is observed (Fig. 3c and 3d). The increase of temperature at the higher pH value (bath D) stabilizes the copper-gluconate complex and Fe deposition is favored while oxygen incorporation is limited (Fig. 3d). The adjustment of the pH weakens the stability of the copper-gluconate complexes and the rise of temperature accelerates copper deposition (bath C). Therefore, at 35°C and 45°C copper is preferentially plated. However, this phenomenon is also marked by a significant elevation of the oxygen amount (Fig. 3c).

Pertaining to bath efficiency, this was found to vary substantially depending on current density and temperature across different electrolytes. Nevertheless, some assessments could be made based on the results from ICP-OES analysis of selected samples for the determination of the Fe and Cu mass deposited experimentally. These were compared to the theoretical mass of Fe and

Cu deposited which was calculated assuming 100% cathodic efficiency using Faraday´s law of electrolysis. In bath D, for example, at a current density of -50 mA cm^{-2} and at a temperature of 35 °C, an overall efficiency of approximately 41% was achieved. In bath C (pH adjusted to 2.2), however, at a current density of -50 mA cm^{-2} and at a temperature of 25 °C, total efficiency dropped to about 11%. Additionally, in bath C, at a current density of -75 mA cm^{-2} and at a temperature of 35 °C, the efficiency was calculated at about 20%. Finally, in bath A, at a current density of -25 mA cm^{-2} and at a temperature of 25 °C, the efficiency was around 18%. Furthermore, based on our observations during electrodeposition, bath D has the highest efficiency for Fe deposition whereas bath B is the most efficient for deposition of Cu. There are optimal current density and temperature combinations in each electrolyte which lead to the highest total efficiency, but these do not follow a linear relationship.

3.3 Surface characterization

From the images obtained using FE-SEM, the dependence of morphology on the plating parameters and electrolyte becomes apparent. Highly copper-rich deposits of approximately 99 at% Cu are granular and smooth with round, closely packed clusters of different size as seen in Fig. 4a. As the copper content decreases, nodular clusters are typically observed, which as is evident in Fig. 4b, are formed much further apart. In the case of Fe-rich deposits from the gluconate electrolyte (bath D), which can be seen in Fig. 4c, the clusters are quite densely packed rendering a cauliflower-like morphology. Finally, Fe-rich deposits from the citric acid and glycine electrolytes tend to grow in the dendritic structure with significant oxygen incorporation (not shown). In any case, it was clear that the incorporation of Fe into Cu deposits brought remarkable changes in morphology.

Results from SEM imaging made it clear that for the Fe-rich samples roughness varied greatly depending on the applied current density and the temperature of the electrolyte. As shown previously, good quality samples with minimized oxygen content were obtained from the gluconate electrolyte at the 4.1 pH value (bath D). Therefore, a closer investigation of roughness variation for these deposits was deemed necessary. The 3D topographical images obtained using the CLSM technique are presented in Fig. 5. It was ascertained that increasing temperature led to gradually much smoother deposits while with respect to the applied current density there was an optimal value of -50 mA cm^{-2}.

Finally, after establishing the optimal conditions required to produce high quality samples with low roughness and minimized oxygen content, it was deemed necessary to further research the oxidation phases present in the Fe-rich deposits and to determine whether oxygen is mostly present at the surface or throughout the entire sample volume. This was investigated by performing XPS analysis on six selected samples with high Fe amount since iron is considerably more prone to oxidation.

The general spectra of one sample chosen as a reference are exhibited in Fig. 6. It can be readily observed that the intensity of the O 1s peak significantly declines after Ar^{+} sputtering. This trend was confirmed for all samples tested. After removal of the surface layer, the Fe and Cu amounts increase accordingly. For added clarity, the atomic percentages of Fe, Cu and O before and after sputtering for all samples are included in Table 1. From the detail spectra of Fe 2p presented in Fig. 7a, the doublets located between 707 eV and 719 eV (2p$_{3/2}$) and between 720 eV and 732 eV (2p$_{1/2}$) with shakeup satellites indicate that Fe is found mostly in an oxidized state (Fe^{2+} and Fe^{3+}). The small shoulder peak observed at around 706.5 eV (2p$_{3/2}$), can be attributed to metallic iron (Fe^{0}). However, after removing the surface by sputtering, the Fe^{0} signal is much stronger, while the oxide peaks decrease. This points to the existence of iron oxide mainly on the surface while after sputtering with Ar^+ ions the main contributions in the XPS spectra correspond to Fe^0. These results are also consistent with EDX quantification due to the large interaction volume in the order of μm in SEM, whereas XPS is very surface sensitive. In the detail spectra of Cu 2p seen in Fig. 7b, the peaks correspond to the Cu^0/Cu^+, Cu^{2+} species and shakeup satellites. The very weak intensity of surface spectra means there is slight amount of Cu, whereas by removing the surface after sputtering, the increased intensity of the peaks associated with Cu^0/Cu^+ suggests that the existent state of Cu is mainly metallic with small amount of oxides. Analysis of O 1s spectra, as presented in Fig. 7c, was performed by comparing with the spectra of Fe and Cu. After sputtering, the oxygen signal sharply decreases and the two main O^{2-} peaks correspond to the Cu oxides while the Fe oxide peak greatly diminishes. Additionally, the contribution from H_2O (533.0 eV) can be found before and after sputtering indicating the absorption of water in the films. Therefore, it can be concluded that the surface was covered mainly by iron and copper oxides and after removal of the surface layer the amount of oxides drastically reduced, thus revealing the metallic states of Fe and Cu.

3.4 Crystallographic structure

The X-ray diffractograms obtained from samples with varying Fe/Cu ratio are illustrated in Fig. 8. The Miller indices of the peaks are also indicated. These results confirm phase separation with clear bcc and fcc peaks for Fe and Cu, respectively.

The XRD patterns were fitted using the Rietveld combined analysis tool provided by the MAUD software. As can be seen from the diffractograms, the films appear textured in the fcc (111) and bcc (110) planes evidenced by the higher relative intensity of these peaks compared to the theoretical intensities of isotropic bcc-Fe and fcc-Cu powders. The theoretical lattice constant for Cu fcc is 3.615 Å [37] and that of Fe bcc is 2.867 Å [38]. As is evident in Table 2, an increase in the amount of Fe is accompanied by a larger bcc volume fraction and a higher Cu amount signifies an elevated fcc volume fraction, respectively. The fcc lattice parameter of copper is also increased, which strongly suggests the inclusion of Fe atoms in the Cu matrix. This makes sense considering the atomic radii of Cu (1.45 Å) and Fe (1.56 Å) atoms. Moreover, it can be seen that the bcc crystallite size is progressively larger at higher bcc volume amounts. There is no clear trend, however, for fcc crystallite size. In any case, the values are within the nanosize domain, likely indicating that saccharine is an effective grain-refining agent in Fe-Cu codeposition. Finally, the microstrains, which is a microstructural parameter expressing the root-mean-square average deviation of the crystal d-spacings often caused by dislocations and other lattice defects, were found to be negligible and, indeed, the films were almost free of cracks. Low microstrains are typically reported in metallic films produced via electrodeposition [39-41], whereas for those produced using mechanical methods (e.g. ball milling) values of the order of 0.01 (or 1%) can be attained [42-44] due to the high dislocation densities resulting from the deformation processes.

3.5 Magnetic properties

Hysteresis loops of deposits with diverse at% Fe were recorded by VSM. The results of these measurements, for fields applied parallel to the film plane, are presented in Fig. 9. The y axis of magnetization has been normalized in emu g^{-1}. As is evident in the graph, the saturation magnetization, M_S, decreases monotonically as the Fe amount is gradually diminished. Note that M_S for pure Fe at room temperature is 217.2 emu g^{-1}. The obtained results are in good agreement with other experimental works on the magnetic properties of FeCu in the literature [8].

Importantly, films with a 6 at% Fe exhibit ferromagnetic behavior albeit with a very low saturation magnetization (~4 emu g^{-1}). This is probably due to the occurrence of phase separation since fully alloyed fcc films with 6 at% Fe are typically paramagnetic at room temperature [13], although an enhanced magnetization is expected at low temperature for fcc-CuFe clusters with very small sizes [45]. Note that a 2-3% bcc-Fe (not detectable by XRD) would be enough to give this small value of M_S. In addition, it is not possible to completely rule out that a small contribution to M_S could come from the presence of ferrimagnetic surface iron oxides, as detected by XPS. Additionally, the films were found to be magnetically isotropic since similar hysteresis loops were recorded when applying the field along the in-plane and out-of-plane directions. The overall low coercivity values recorded (~42-154 Oe) classify this material as soft magnetic and could find applications as structural components in magnetic micro- and nano-electromechanical systems (MEMS/NEMS).

4. Conclusions

In this work, Fe_xCu_{1-x} films were deposited within a wide composition range and the effect of three different complexing agents as well as of various plating conditions were systematically investigated. Subsequently, detailed morphological, structural and magnetic characterization was carried out. The choice of complexing agent was crucial in determining the derivable stoichiometry and the span of current densities leading to good adhesion and high film quality. Gluconate as a complexing agent leads to Fe-rich films because of suppression of Cu deposition, while in the case of citric acid and glycine higher current density favors Fe deposition. The increase of temperature typically favors Cu inclusion, although in the case of the gluconate electrolyte at the 4.1 pH value the effect is negligible. Film morphology is nodular with cauliflower-like cluster formation. In terms of roughness, higher temperature leads to smoother deposits with more densely packed clusters. Current density is also critical factor and an optimal value of -50 mA cm^{-2} can be reported for the gluconate electrolyte. Oxygen is mostly found at the uppermost layer of the deposits where it most likely forms a passivation layer. Magnetite Fe_3O_4 and hematite Fe_2O_3 are the oxide phases present in the films. From the results of structural analysis, phase separation was confirmed with clear bcc and fcc diffraction peaks. However, the findings from Rietveld refinement strongly indicate partial alloying. Magnetic hysteresis measurements of the films revealed that saturation magnetization can be tuned by configuration of the at% Fe and, in contrast to previous studies, a low magnetic moment was observed even in the case of diminished Fe content.

Acknowledgements

This work was supported by the SELECTA (No. 642642) H2020-MSCA-ITN-2014 project**.** Partial financial support by the Spanish Government [Project MAT2014-57960- C3-1-R and associated FEDER], the Generalitat de Catalunya (2014-SGR- 1015) and the European Research Council (SPIN-PORICS 2014-Consolidator Grant, Agreement nº 648454) is acknowledged. E.P. is grateful to MINECO for the “Ramon y Cajal” contract (RYC-2012-10839).

References

[1] Tsunoda, Y., Kunitomi, N. and Nicklow, R.M., 1987. Magnetic structure of γ-Fe precipitates in a Cu matrix. *Journal of Physics F: Metal Physics*, *17*(12), p.2447.

[2] Tsunoda, Y., 1989. Spin-density wave in cubic γ-Fe and γ-$Fe_{100-x}Co_x$ precipitates in Cu. *Journal of Physics: Condensed Matter*, *1*(51), p.10427.

[3] Gorria, P., Martínez-Blanco, D., Blanco, J.A., Pérez, M.J., Hernando, A., Barquín, L.F. and Smith, R.I., 2005. High-temperature induced ferromagnetism on γ−Fe precipitates in FeCu solid solutions. *Physical Review B*, *72*(1), p.014401.

[4] Macedo, W.A.A. and Keune, W., 1988. Magnetism of epitaxial fcc-Fe (100) films on Cu (100) investigated in situ by conversion-electron Mössbauer spectroscopy in ultrahigh vacuum. *Physical Review Letters*, *61*(4), p.475.

[5] Li, D., Freitag, M., Pearson, J., Qiu, Z.Q. and Bader, S.D., 1994. Magnetic phases of ultrathin Fe grown on Cu (100) as epitaxial wedges. *Physical Review Letters*, *72*(19), p.3112.

[6] Kaufman, L., 1978. Coupled phase diagrams and thermochemical data for transition metal binary systems-III. *Calphad*, *2*(2), pp.117-146.

[7] Hansen, M., Anderko, K. and Salzberg, H.W., 1958. Constitution of binary alloys. *Journal of the Electrochemical Society*, *105*(12), pp.260C-261C.

[8] Yavari, A.R., Desre, P.J. and Benameur, T., 1992. Mechanically driven alloying of immiscible elements. *Physical Review Letters*, *68*(14), p.2235.

[9] Eckert, J., Holzer, J.C. and Johnson, W.L., 1993. Thermal stability and grain growth behavior of mechanically alloyed nanocrystalline Fe–Cu alloys. *Journal of Applied Physics*, *73*(1), pp.131-141.

[10] Harris, V.G., Kemner, K.M., Das, B.N., Koon, N.C., Ehrlich, A.E., Kirkland, J.P., Woicik, J.C., Crespo, P., Hernando, A. and Escorial, A.G., 1996. Near-neighbor mixing and bond dilation in mechanically alloyed Cu-Fe. *Physical Review B*, *54*(10), p.6929.

[11] Schilling, P.J., He, J.H., Cheng, J. and Ma, E., 1996. Extended x–ray absorption fine structure of metastable bcc and fcc phases in mechanically alloyed Fe–Cu. *Applied Physics Letters*, *68*(6), pp.767-769.

[12] Wanderka, N., Czubayko, U., Naundorf, V., Ivchenko, V.A., Yermakov, A.Y., Uimin, M.A. and Wollenberger, H., 2001. Characterization of nanoscaled heterogeneities in mechanically alloyed and compacted CuFe. *Ultramicroscopy*, *89*(1), pp.189-194.

[13] Gorria, P., Martínez-Blanco, D., Blanco, J.A., Hernando, A., Garitaonandia, J.S., Barquín, L.F., Campo, J. and Smith, R.I., 2004. Invar effect in fcc-FeCu solid solutions. *Physical Review B*, *69*(21), p.214421.

[14] Bachmaier, A., Kerber, M., Setman, D. and Pippan, R., 2012. The formation of supersaturated solid solutions in Fe–Cu alloys deformed by high-pressure torsion. *Acta Materialia*, *60*(3), pp.860-871.

[15] Chien, C.L., Liou, S., Kofalt, D., Yu, W., Egami, T., Watson, T.J. and McGuire, T.R., 1986. Magnetic properties of Fe_xCu_{100-x} solid solutions. *Physical Review B, 33*(5), p.3247.

[16] Kuch, W., Salvietti, M., Gao, X., Lin, M.T., Klaua, M., Barthel, J., Mohan, C.V. and Kirschner, J., 1998. Artificially ordered FeCu alloy superlattices on Cu (001). II. Spin-resolved electronic properties and magnetic dichroism. *Physical Review B, 58*(13), p.8556.

[17] Desautels, R.D., Shueh, C., Lin, K.W., Freeland, J.W. and van Lierop, J., 2016. Dynamical freezing, magnetic ordering, and the magnetocaloric effect in nanostructured Fe/Cu thin films. *Applied Physics Letters*, *108*(17), p.172410.

[18] Tian, Z., Tian, C.S., Yin, L.F., Wu, D., Dong, G.S., Jin, X. and Qiu, Z.Q., 2004. Magnetic ordering and anisotropy of epitaxially grown Fe_xCu_{1-x} alloy on GaAs (001). *Physical Review B*, *70*(1), p.012301.

[19] Bakkaloğlu, Ö.F., 1998. A magnetic study of sputtered Fe/Cu multilayer films. *Journal of Magnetism and Magnetic Materials*, *182*(3), pp.324-328.

[20] Roig, A., Zhang, X.X., Żuberek, R., Tejada, J. and Molins, E., 1995. Magnetic properties of FeCu multilayers. *Journal of Magnetism and Magnetic Materials*, *140*, pp.559-560.

[21] Sakai, T., Oomi, G., Okada, K., Takanashi, K., Saito, K. and Fujimori, H., 1997. Effect of pressure on the giant magnetoresistance of Fe/Cu magnetic multilayer. *Physica B: Condensed Matter*, *237*, pp.275-277.

[22] Schreiner, W.H., Mosca, D.H., Teixeira, S.R. and Mattoso, N., 1992. Epitaxial Fe/Cu superlattices on Si (111). *Journal of Applied Physics*, *72*(12), pp.5682-5686.

[23] Ueda, Y. and Kikuchi, N., 1993. Structure and magnetic properties of electrodeposited Fe-Cu alloy films. *Japanese Journal of Applied Physics*, *32*(4R), p.1779.

[24] Williams, J.M., Blythe, H.J. and Fedosyuk, V.M., 1996. An investigation of electrodeposited granular CuFe alloyed films. *Journal of Magnetism and Magnetic Materials*, *155*(1), pp.355-357.

[25] Revenko, V.G., Pershutin, V.V., Shkurpelo, A.I., Chernova, G.P. and Bogdashkina, N.L., 2002. Electroplating of Iron–Copper Coatings. *Protection of Metals*, *38*(4), pp.377-381.

[26] Roy, M.K. and Verma, H.C., 2004. Mössbauer studies of Fe–Cu alloys prepared by electrodeposition. *Journal of Magnetism and Magnetic Materials*, *270*(1), pp.186-193.

[27] Noce, R.D., Gomes, O.D.M., de Magalhães, S.D., Wolf, W., Guimarães, R.B., De Castro, A.C., Pires, M.J.M., Macedo, W.A.A., Givord, D. and Barthem, V.M.T.S., 2009.

Magnetic properties of Fe-Cu alloys prepared by pulsed electrodeposition. *Journal of Applied Physics*, *106*(9), p.93907.

[28] Verma, H.C., 2007. Mössbauer studies of CuFe-72% alloy. *Indian Journal of Pure and Applied Physics*, *45*(10), pp.851-855.

[29] Lange, G.A., Eugénio, S., Duarte, R.G., Silva, T.M., Carmezim, M.J. and Montemor, M.D.F., 2015. Characterisation and electrochemical behaviour of electrodeposited Cu–Fe foams applied as pseudocapacitor electrodes. *Journal of Electroanalytical Chemistry*, *737*, pp.85-92.

[30] Merikhi, M., Nabiyouni, G. and Ghanbari, B., 2015. Effect of Magnetic Field on Surface Morphology and Magnetic Properties of FeCu/Cu Nano layers Prepared by Electrodeposition Technique: Investigation of Magneto-hydrodynamic Effect. *Journal of Nanostructures*, *5*(4), pp.409-414.

[31] Lutterotti, L., and Scardi, P., 1990. Simultaneous structure and size–strain refinement by the Rietveld method. *Journal of Applied Crystallography*, *23*(4), pp.246-252.

[32] Repoux, M., 1992. Comparison of background removal methods for XPS. *Surface and Interface Analysis*, *18*(7), pp.567-570.

[33] Tabakovic, I., Riemer, S., Jayaraju, N., Venkatasamy, V. and Gong, J., 2011. Relationship of Fe^{2+} concentration in solution and current efficiency in electrodeposition of CoFe films. *Electrochimica Acta*, *58*, pp.25-32.

[34] El Rehim, S.A., Sayyah, S.M. and El Deeb, M.M., 2000. Electroplating of copper films on steel substrates from acidic gluconate baths. *Applied Surface Science*, *165*(4), pp.249-254.

[35] Rode, S., Henninot, C., Vallières, C. and Matlosz, M., 2004. Complexation chemistry in copper plating from citrate baths. *Journal of the Electrochemical Society*, *151*(6), pp.C405-C411.

[36] Ballesteros, J.C., Chainet, E., Ozil, P., Meas, Y. and Trejo, G., 2011. Electrocristallization of copper from non-cyanide alkaline solution containing glycine. *Int. J. Electrochem. Sci*, *6*, pp.1597-1616.

[37] Otte, H.M., 1961. Lattice Parameter Determinations with an X‐Ray Spectrogoniometer by the Debye‐Scherrer Method and the Effect of Specimen Condition. *Journal of Applied Physics*, *32*(8), pp.1536-1546.

[38] Woodward, P.M., Suard, E. and Karen, P., 2003. Structural tuning of charge, orbital, and spin ordering in double-cell perovskite series between $NdBaFe_2O_5$ and $HoBaFe_2O_5$. *Journal of the American Chemical Society*, *125*(29), pp.8889-8899.

[39] Lu, L., Tao, N.R., Wang, L.B., Ding, B.Z. and Lu, K., 2001. Grain growth and strain release in nanocrystalline copper. *Journal of Applied Physics*, *89*(11), pp.6408-6414.

[40] Mahalingam, T., Chitra, J.S.P., Chu, J.P. and Sebastian, P.J., 2004. Preparation and microstructural studies of electrodeposited Cu 2 O thin films. *Materials letters*, *58*(11), pp.1802-1807.

[41] Mahalingam, T., John, V.S. and Hsu, L.S., 2007. Microstructural analysis of electrodeposited zinc oxide thin films. *Journal of New Materials for Electrochemical Systems*, *10*(1), p.9.

[42] Lucas, F.M., Trindade, B., Costa, B.F. and Le Caër, G., 2002. Mechanical alloying of Fe-Cu alloys from As-received and premilled elemental powder mixtures. In *Key Engineering Materials* (Vol. 230, pp. 631-634). Trans Tech Publications.

[43] Gorria, P., Martínez-Blanco, D., Blanco, J.A., Pérez, M.J., González, M.A. and Campo, J., 2006. Magnetism and structure of Fe–Cu binary solid solutions obtained by high-energy ball milling. *Physica B: Condensed Matter*, *384*(1), pp.336-340.

[44] Krifa, M., Mhadhbi, M., Escoda, L., Saurina, J., Suñol, J.J., Llorca-Isern, N., Artieda-Guzmán, C. and Khitouni, M., 2013. Phase transformations during mechanical alloying of Fe–30% Al–20% Cu. *Powder technology*, *246*, pp.117-124.

[45] Cutrano, C. and Lekka, C., 2016. Structural, magnetic and electronic properties of Cu-Fe nanoclusters by density functional theory calculations. *Journal of Alloys and Compounds*, In press.

Figure Captions

Fig. 1. Cyclic voltammetries under stirring conditions from (a) electrolyte A with omission of the Cu salt (b) electrolyte A at different cathodic limits (c) electrolytes A, B and C at 25˚C and (d) electrolyte C at different temperatures.

Fig. 2. Deposit composition dependence on current density at 25 ˚C for different electrolytes: (a) bath A (b) bath B (c) bath C (d) bath D.

Fig. 3. Deposit composition dependence on temperature for different electrolytes: (a) bath A (b) bath B (c) bath C (d) bath D for deposits plated at a current density of -50 mA cm^{-2}.

Fig. 4. Representative SEM images of films of distinct composition (a) almost pure Cu (99 at%) deposit obtained from bath B at 25 mA cm^{-2} current density at 25 ˚C with a 36 min deposition time (b) $Fe_{34}Cu_{66}$ from bath A at -50 mA cm^{-2} at 45 ˚C with an 18 min deposition time (c) $Fe_{74}Cu_{14}$ from bath D at -50 mA cm^{-2} at 45 ˚C with an 18 min deposition time.

Fig. 5. CLSM 3D images illustrating roughness variation of Fe-rich films deposited from bath D at different current densities and temperatures: (a) $Fe_{90}Cu_{10}$, -25 mA cm^{-2} (left) and $Fe_{88}Cu_{12}$, -50 mA cm^{-2} (right) at 25˚C (b) $Fe_{78}Cu_{22}$, -25 mA cm^{-2} (top left), $Fe_{88}Cu_{12}$, -50 mA cm^{-2} (bottom left) and $Fe_{92}Cu_{8}$, -75 mA cm^{-2} (bottom right) at 35˚C (c) $Fe_{71}Cu_{29}$, -25 mA cm^{-2} (top left), $Fe_{84}Cu_{16}$, -50 mA cm^{-2} (bottom left) and $Fe_{86}Cu_{14}$, -75 mA cm^{-2} (bottom right) at 45˚C.

Fig. 6. XPS general surface profile of Fe-rich reference sample before (red curve) and after 2 min Ar^+ sputtering (blue curve).

Fig. 7. Experimental and deconvoluted detail spectra at surface (left) and at ~10 - 15 nm below surface layer (right) of (a) Fe 2p, (b) Cu 2p and (c) O 1s bands of reference sample.

Fig. 8. X-ray Diffraction patterns for films of varying composition.

Fig. 9. Magnetic hysteresis loops obtained from films of varying Fe content. The inset shows a magnified detail at low fields.

Fig. 1

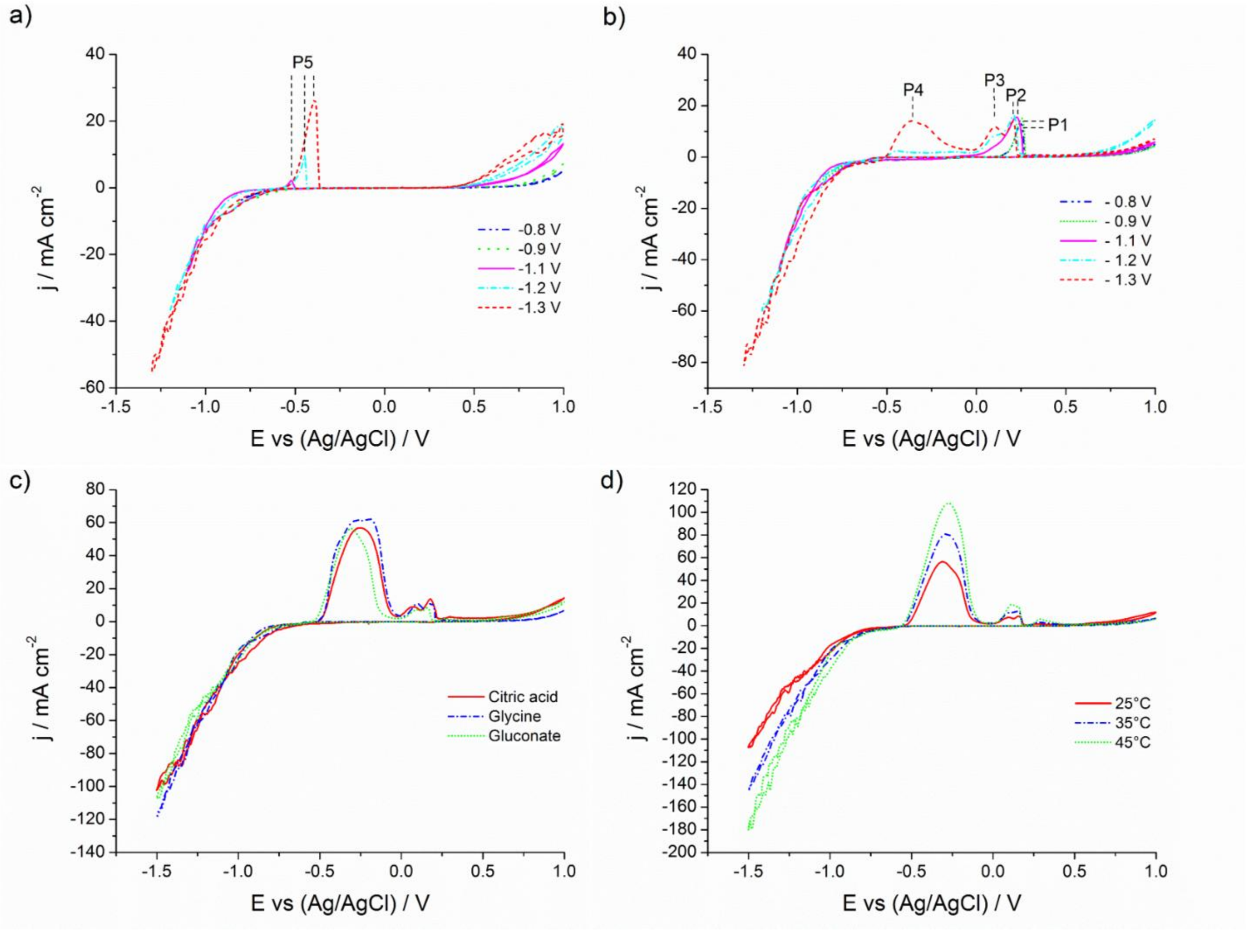
a)
P5
j / mA cm^{-2}
40
20
0
-20
-40
-60
-1.5
-1.0
-0.5
0.0
0.5
1.0
E vs (Ag/AgCl) / V
-0.8 V
-0.9 V
-1.1 V
-1.2 V
-1.3 V
b)
P4
P3
P2
P1
j / mA cm^{-2}
40
20
0
-20
-40
-60
-80
-1.5
-1.0
-0.5
0.0
0.5
1.0
E vs (Ag/AgCl) / V
- 0.8 V
- 0.9 V
- 1.1 V
- 1.2 V
- 1.3 V
c)
j / mA cm^{-2}
80
60
40
20
0
-20
-40
-60
-80
-100
-120
-140
-1.5
-1.0
-0.5
0.0
0.5
1.0
E vs (Ag/AgCl) / V
Citric acid
Glycine
Gluconate
d)
j / mA cm^{-2}
120
100
80
60
40
20
0
-20
-40
-60
-80
-100
-120
-140
-160
-180
-200
-1.5
-1.0
-0.5
0.0
0.5
1.0
E vs (Ag/AgCl) / V
25°C
35°C
45°C

Fig. 2

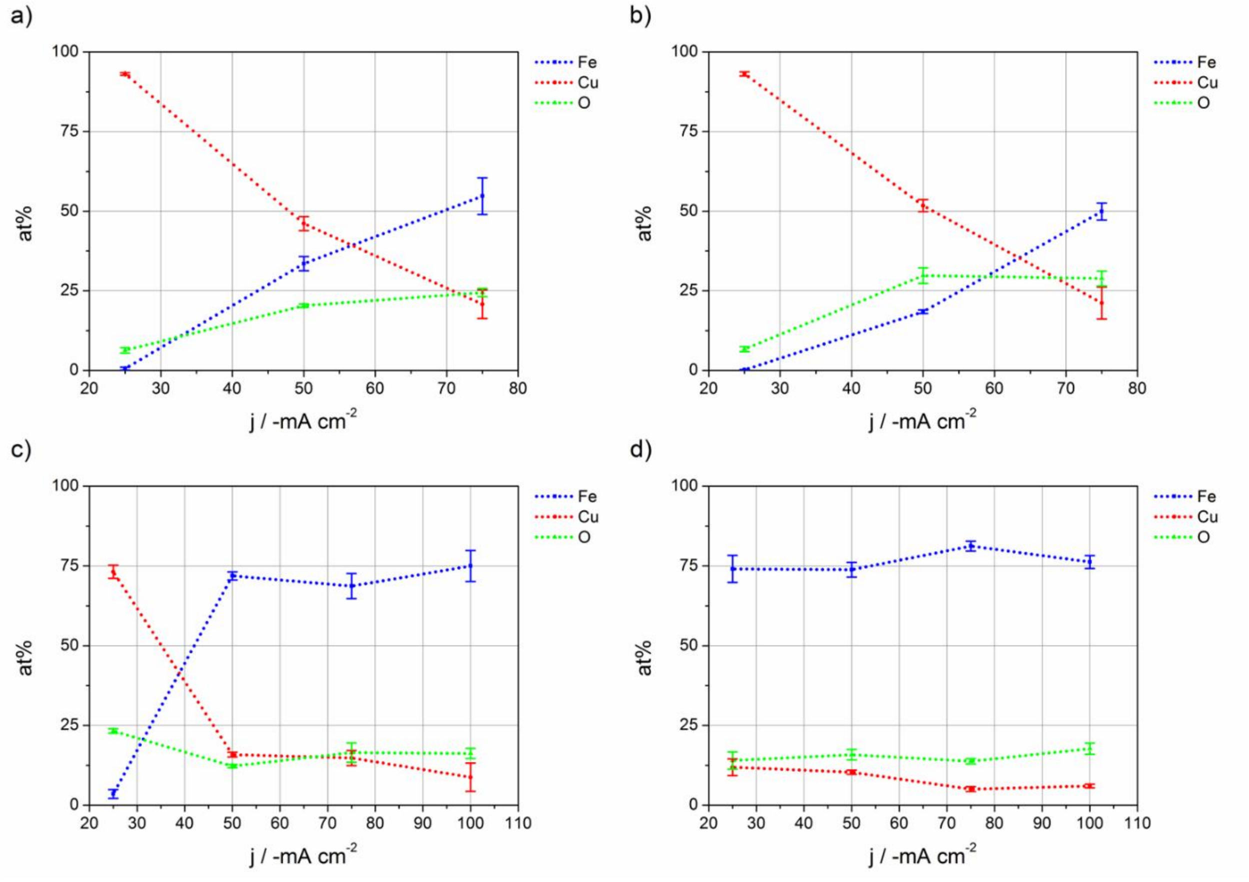

Fig. 3

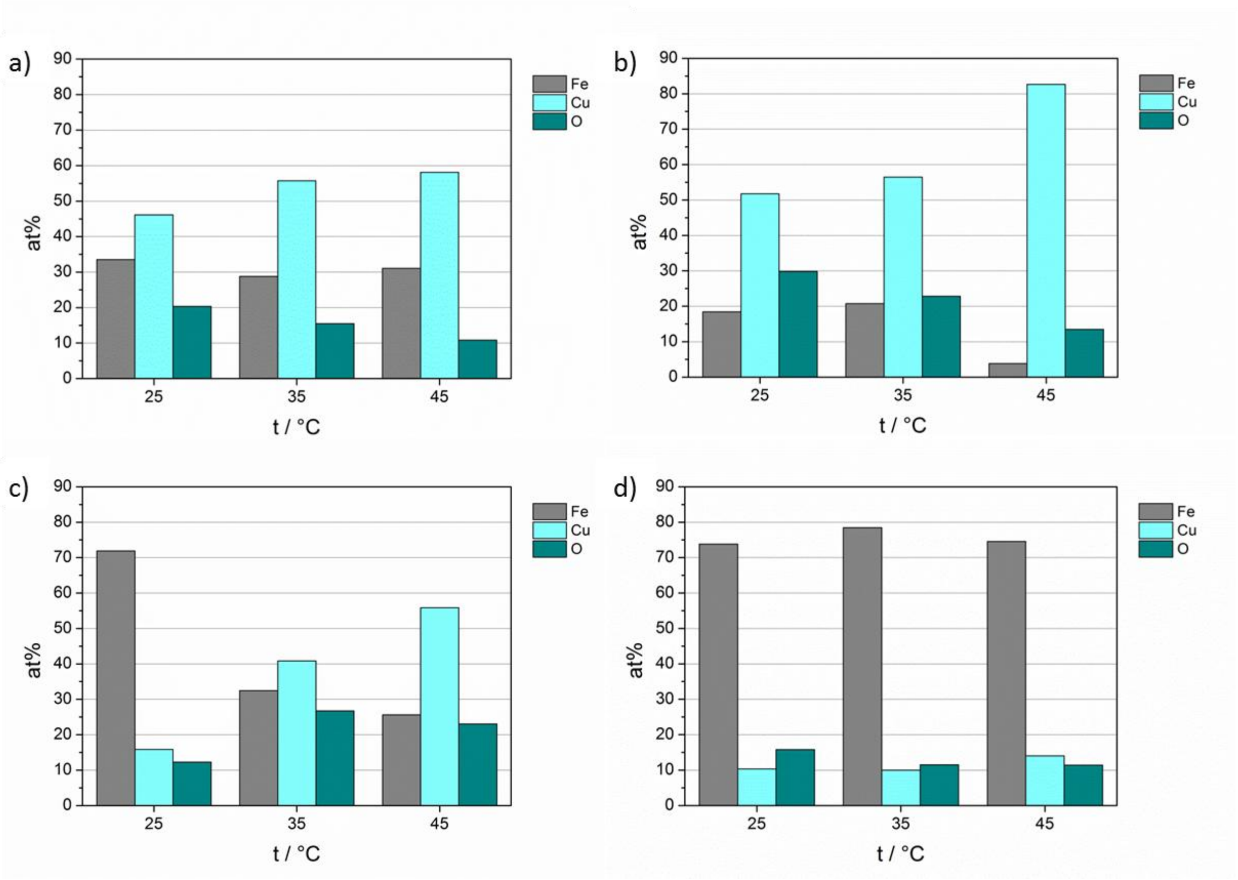

Fig. 4

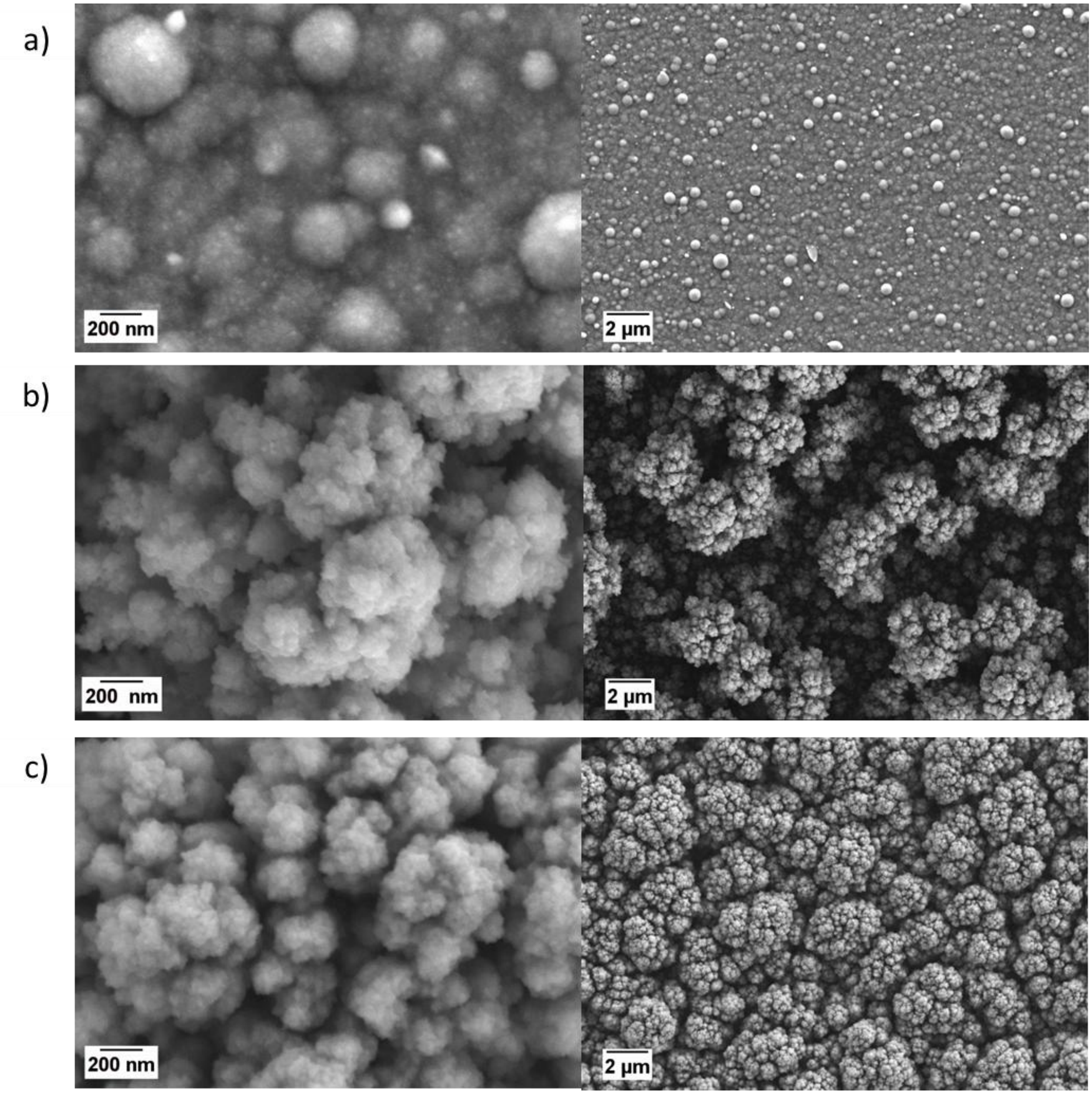

Fig. 5

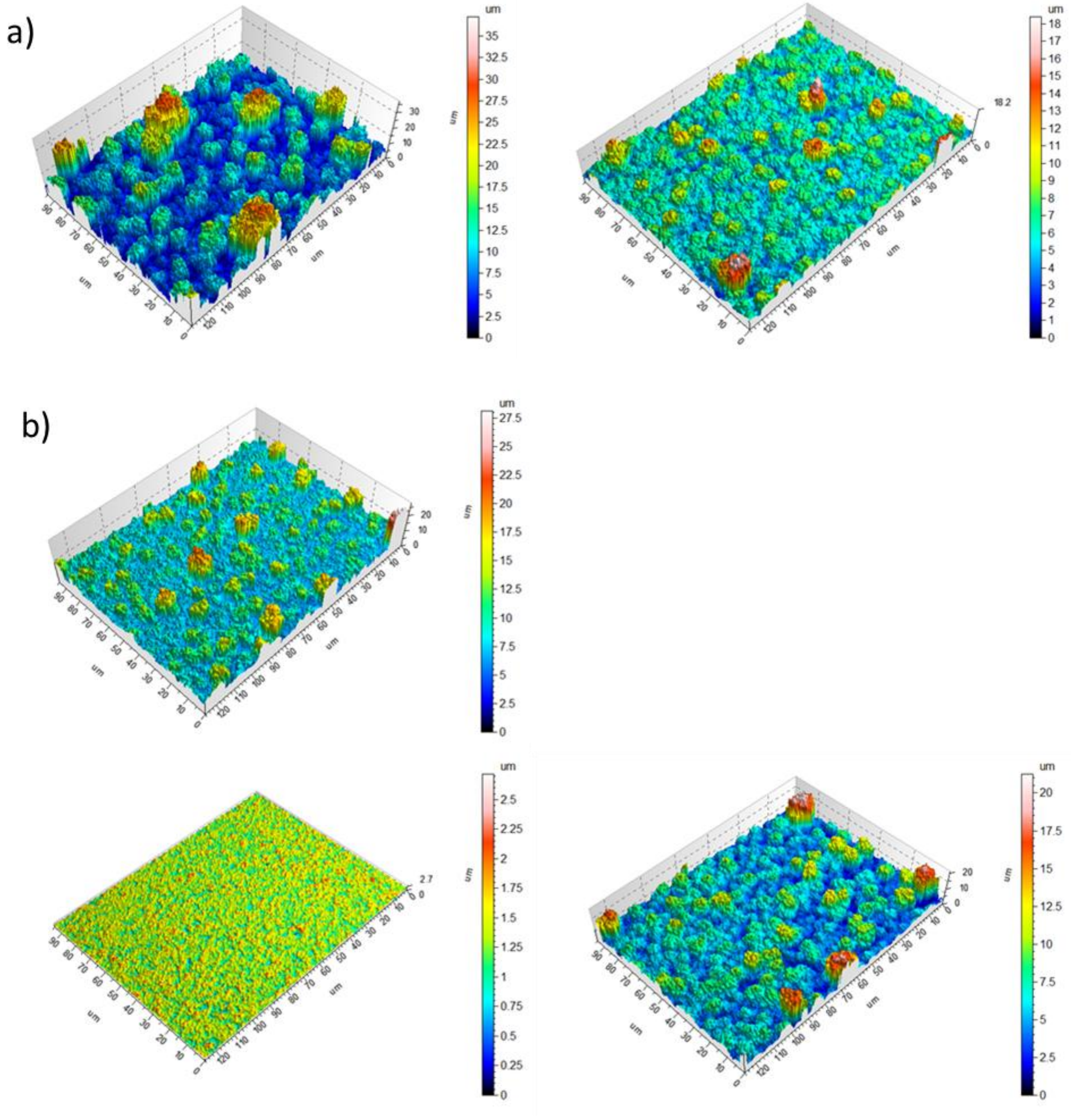
a)
b)
um
0
2.5
5
7.5
10
12.5
15
17.5
20
22.5
25
27.5
30
32.5
35
18.2
2.7
0.25
0.5
0.75
1
1.25
1.5
1.75
2
2.25
2.5

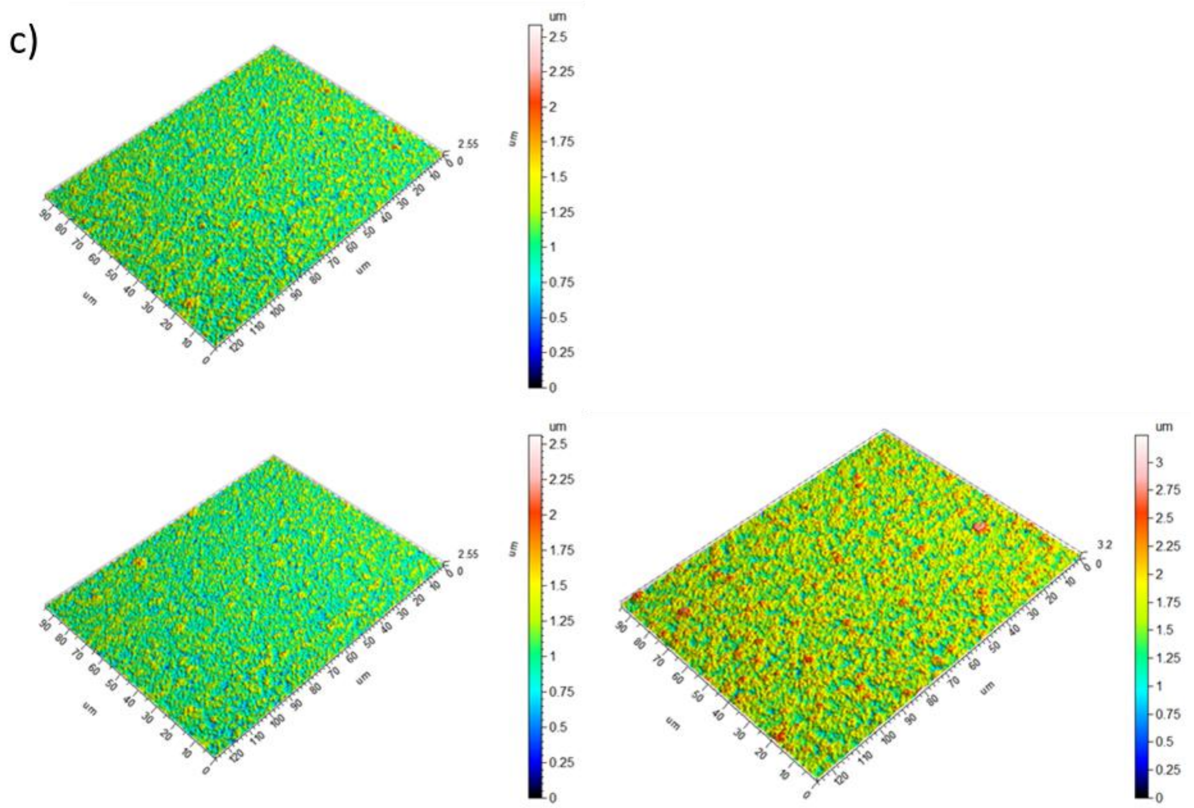
c)
um
2.5
2.25
2
1.75
1.5
1.25
1
0.75
0.5
0.25
0
2.55
0
um
10 20 30 40 50 60 70 80 90 100 110 120
um
0 10 20 30 40 50 60 70 80 90
um
3
2.75
2.5
2.25
2
1.75
1.5
1.25
1
0.75
0.5
0.25
0
3.2
0

Fig. 6

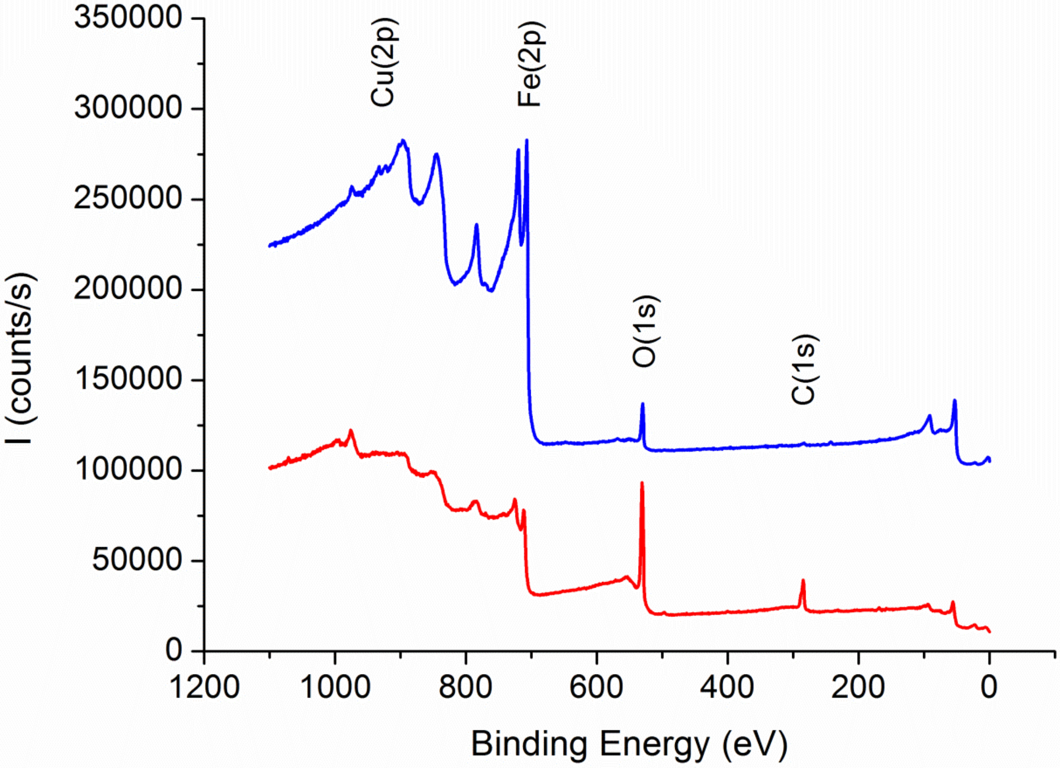
350000
300000
250000
200000
150000
100000
50000
0
I (counts/s)
1200
1000
800
600
400
200
0
Binding Energy (eV)
Cu(2p)
Fe(2p)
O(1s)
C(1s)

Fig. 7

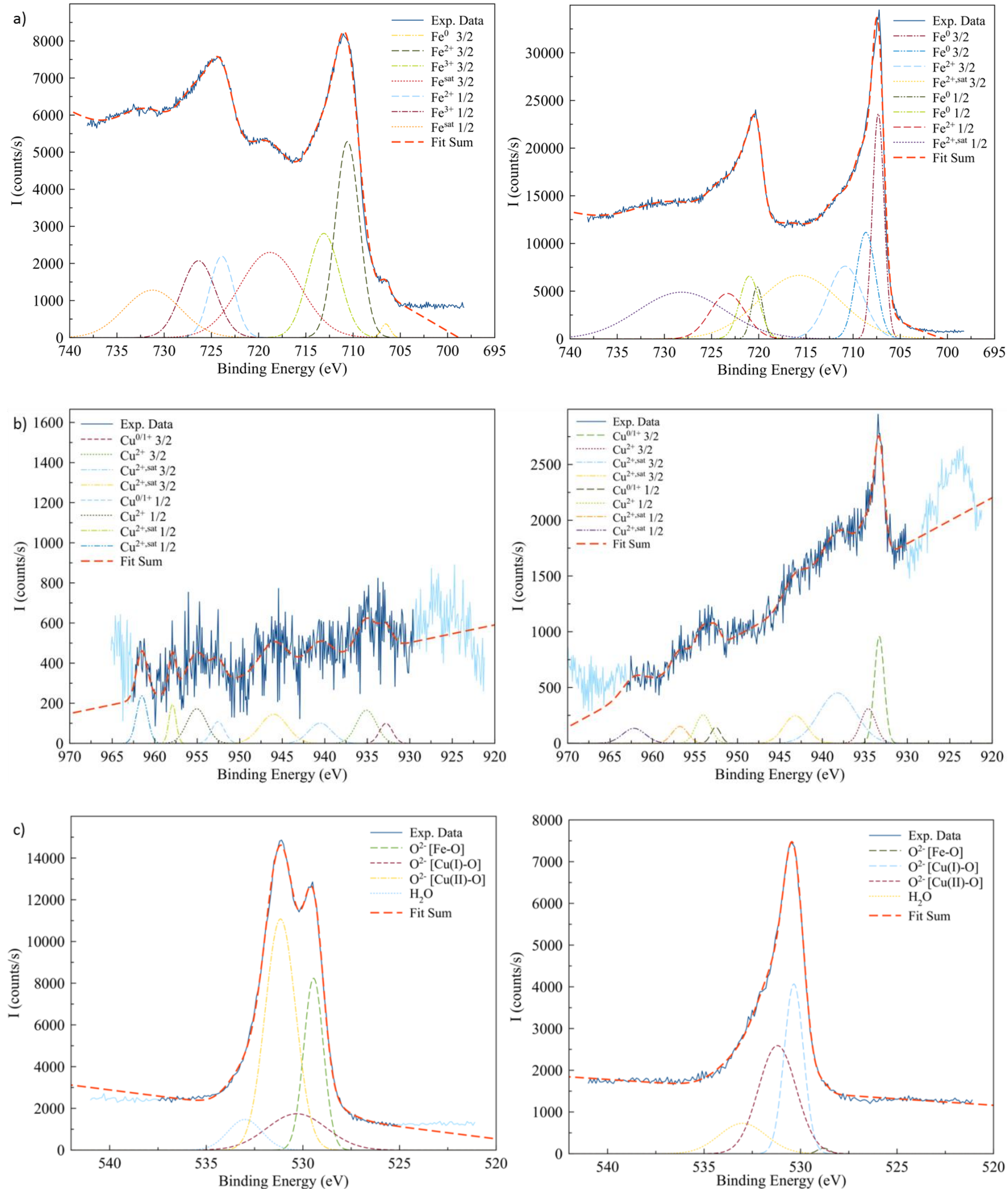
a)
Exp. Data
Fe^0 3/2
Fe^{2+} 3/2
Fe^{3+} 3/2
Fe^{sat} 3/2
Fe^{2+} 1/2
Fe^{3+} 1/2
Fe^{sat} 1/2
Fit Sum
I (counts/s)
0
1000
2000
3000
4000
5000
6000
7000
8000
Binding Energy (eV)
740
735
730
725
720
715
710
705
700
695
Exp. Data
Fe^0 3/2
Fe^0 3/2
Fe^{2+} 3/2
$Fe^{2+,sat}$ 3/2
Fe^0 1/2
Fe^0 1/2
Fe^{2+} 1/2
$Fe^{2+,sat}$ 1/2
Fit Sum
I (counts/s)
0
5000
10000
15000
20000
25000
30000
Binding Energy (eV)
b)
Exp. Data
$Cu^{0/1+}$ 3/2
Cu^{2+} 3/2
$Cu^{2+,sat}$ 3/2
$Cu^{2+,sat}$ 3/2
$Cu^{0/1+}$ 1/2
Cu^{2+} 1/2
$Cu^{2+,sat}$ 1/2
$Cu^{2+,sat}$ 1/2
Fit Sum
I (counts/s)
0
200
400
600
800
1000
1200
1400
1600
Binding Energy (eV)
970
965
960
955
950
945
940
935
930
925
920
Exp. Data
$Cu^{0/1+}$ 3/2
Cu^{2+} 3/2
$Cu^{2+,sat}$ 3/2
$Cu^{2+,sat}$ 3/2
$Cu^{0/1+}$ 1/2
Cu^{2+} 1/2
$Cu^{2+,sat}$ 1/2
$Cu^{2+,sat}$ 1/2
Fit Sum
I (counts/s)
0
500
1000
1500
2000
2500
Binding Energy (eV)
c)
Exp. Data
O^{2-} [Fe-O]
O^{2-} [Cu(I)-O]
O^{2-} [Cu(II)-O]
H_2O
Fit Sum
I (counts/s)
0
2000
4000
6000
8000
10000
12000
14000
Binding Energy (eV)
540
535
530
525
520
Exp. Data
O^{2-} [Fe-O]
O^{2-} [Cu(I)-O]
O^{2-} [Cu(II)-O]
H_2O
Fit Sum
I (counts/s)
0
1000
2000
3000
4000
5000
6000
7000
8000
Binding Energy (eV)

Fig. 8

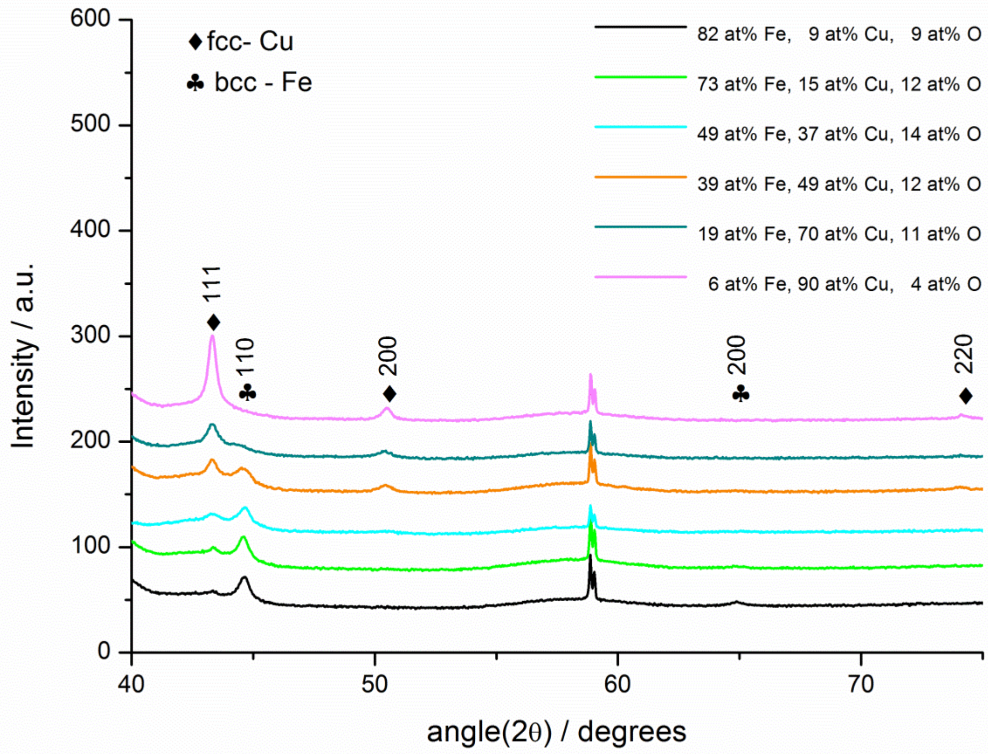
600
500
400
300
200
100
0
Intensity / a.u.
40
50
60
70
angle(2θ) / degrees
♦ fcc- Cu
♣ bcc - Fe
82 at% Fe, 9 at% Cu, 9 at% O
73 at% Fe, 15 at% Cu, 12 at% O
49 at% Fe, 37 at% Cu, 14 at% O
39 at% Fe, 49 at% Cu, 12 at% O
19 at% Fe, 70 at% Cu, 11 at% O
6 at% Fe, 90 at% Cu, 4 at% O
♦ 111
♣ 110
♦ 200
♣ 200
♦ 220

Fig. 9

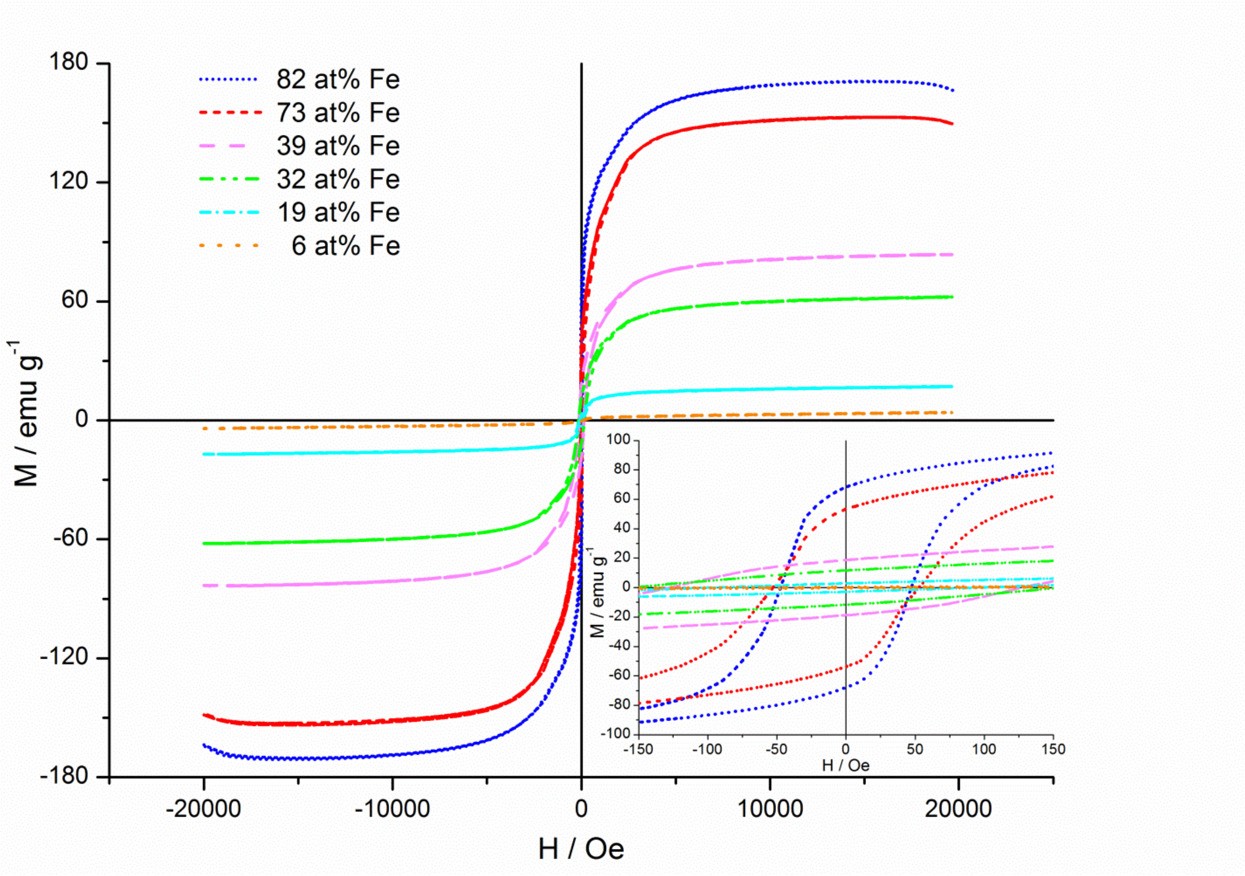

82 at% Fe
73 at% Fe
39 at% Fe
32 at% Fe
19 at% Fe
6 at% Fe
M / emu g^{-1}
H / Oe
180
120
60
0
-60
-120
-180
-20000
-10000
0
10000
20000
100
80
60
40
20
-20
-40
-60
-80
-100
-150
-100
-50
50
100
150

Table 1. Atomic percentage of elements determined via XPS before and after surface sputtering.

At% Before Sputtering			**At% After Sputtering**		
Fe	**Cu**	**O**	**Fe**	**Cu**	O
26.80	0.27	72.93	81.93	1.28	16.79
28.69	0.66	70.65	76.70	2.36	20.95
21.16	15.51	63.33	72.45	8.93	18.62
27.07	4.47	68.45	63.47	6.96	29.57
29.74	2.72	67.55	76.74	3.70	19.56
30.72	13.14	56.14	76.52	11.98	11.49

Table 2. Lattice parameters, crystallite size and microstrains of films of diverse compositions.

Composition according to EDX	**Volume Fraction**	**Lattice Constant a**		**Crystallite Size**		**Microstrains**	
		Fe-bcc (Å)	**Cu-fcc (Å)**	**Fe-bcc (nm)**	**Cu-fcc (nm)**	**Fe-bcc**	**Cu-fcc**
90 at% Fe 10 at% Cu	bcc:0.86 fcc:0.14	2.87702	3.63471	30.8	69.0	1.30×10^{-5}	5.08×10^{-7}
83 at% Fe 17 at% Cu	bcc:0.71 fcc:0.29	2.88396	3.63591	29.4	75.0	1.18×10^{-7}	7.70×10^{-5}
57 at% Fe 43 at% Cu	bcc:0.67 fcc:0.33	2.87110	3.62152	22.4	8.5	1.81×10^{-6}	5.56×10^{-6}
44 at% Fe 56 at% Cu	bcc:0.50 fcc:0.50	2.87632	3.62001	15.3	16.9	1.78×10^{-6}	6.25×10^{-7}
21 at% Fe 79 at% Cu	bcc:0.36 fcc:0.64	2.89166	3.62725	9.4	20.5	4.74×10^{-6}	7.45×10^{-6}
6 at% Fe 94 at% Cu	bcc:0.17 fcc:0.83	2.88664	3.61038	7.3	48.5	4.17×10^{-7}	2.03×10^{-6}